Particle-scale simulations of the compression and shearing of kaolin clay

John de Bono University of Nottingham
Glenn McDowell University of Nottingham

ABSTRACT

This paper presents a new model for particle-scale simulations of clay. Using the discrete element method (DEM), featuring realistically-shaped platelets with separate interactions between the various platelet surfaces, simulations of isotropic normal compression and triaxial shearing are performed. A normal compression line is established, and for the first time so is a critical state line, which is parallel to the normal compression line in *e*-log *p* space. The critical state line is obtained from conventional, constant mean stress, and constant volume tests on normally consolidated and overconsolidated samples. The critical state line appears linear in *q*-*p* space and the first insights into a state boundary surface for the clay are established. This new model appears capable of capturing the key features of macroscopic clay behaviour.

INTRODUCTION

This paper presents a new particle-scale model capable of reproducing all important aspects of clay behaviour. Numerical tools such as the discrete element method (DEM) or molecular dynamics have long been used to simulate the behaviour of particulate materials, leading to many useful insights; however these tools are yet to be applied to their full potential investigating more complex materials such as clay.

Using DEM (or the closely-related molecular dynamics) to model very fine-grained materials like clays is problematic due to the fact that clay mineral particles experience complex interactions and possess shapes which are inefficient to model (and cannot be simplified). For this reason, there have been relatively few attempts at modelling clay using particle-scale simulations. Anandarajah and co-workers were the first to use DEM to model clay platelets; first in 2D (e.g. Anandarajah, 2000) modelling kaolinite platelets as rods, and later in 3D modelling the platelets as cuboids (e.g. Yao and Anandarajah, 2003). These seminal studies, which focussed on simulating one-dimensional compression, laid the foundation for several later studies by others. For example, Bayesteh and co-workers have used two-dimensional rods to simulate the compression and swelling of clays (e.g. Bayesteh and Hoseini, 2021; Khabazian et al., 2018). Using disks, Ebrahimi et al. (2016) investigated the aggregation of montmorillonite platelets, while Bandera et al.

(2021) used disks to simulate the one-dimensional compression of kaolinite platelets. Other researchers have used rigid assemblies of spheres to model kaolinite platelets: such as Guo and Yu (2019) who investigated sedimentation; Sjoblom (2015) and Pagano et al. (2020), who both simulated the normal compression of kaolin; and Aminpour and Sjoblom (2019) who simulated triaxial shear tests.

In addition to the variety of methods used to model platelet shape, most of the above studies also used different approaches to modelling the particle interactions. Whilst this variety provides an excellent basis for the development of more advanced simulations, it must be noted that these past models had a number of shortcomings, limiting their ability to reproduce keys aspects of clay behaviour. For instance, most of these studies have focused on modelling kaolinite, however none of the models took into consideration the different faces (silica/alumina) of each platelet; and in those studies that modelled platelets using assemblies of spheres, the interactions were not calibrated, meaning that the platelet—platelet behaviour was unclear. These issues have been highlighted recently in de Bono and McDowell (2023, 2022a).

The work presented here aims to build upon these past numerical models and provide a significant advancement of particle-scale modelling of clays. The numerical model includes innovative features (multifaceted platelets, adhesion-dependent friction), and for the first time simulates the compression and shearing of a clay using a deformable membrane, replicating triaxial conditions. The model is shown to go beyond previous works by reproducing the fundamental features of clay behaviour one would expect: a normal compression line, dilative and contractile behaviour upon shearing, and a critical state line (which is parallel to the normal compression line).

NUMERICAL MODEL

Platelets

Following on from the majority of previous attempts, this numerical study focuses on simulating kaolin. This is due to the wealth of experimental data available for this material, which allows focussing on the numerical modelling. Real kaolinite platelets are flat, approximately hexagonal, with platelet diameters typically in the range 0.1–4.0 μm and with aspect ratios between 5–100 (Mitchell and Soga, 2005).

In this DEM study, the kaolinite platelets are modelled using rigid arrays of spheres (Figure 1). Broadly speaking, there are two ways of modelling non-spherical particles in DEM: by using rigid arrays of smaller spheres, or by using convex polyhedrons. Using convex polyhedrons has the advantage of fewer bodies for which to compute motion, and fewer interactions. However, a pair of convex bodies may usually only have a single contact (or interaction) existing between them—and it is not practicable to define a single interaction law that explicitly accounts for the distinct surfaces as well as arbitrary orientations of the platelets. In contrast, using multiple spheres to model each particle means multiple interactions are computed between the constituent spheres in any two neighbouring platelets. This makes it relatively easy to implement different types of interactions between different surfaces of the platelets, and automatically accounts for platelet orientations. Accordingly, modelling platelets using multiple spheres should be considered as a convenient means to achieve (i) the correct particle shape, (ii) the desired interactions between different platelet surfaces. This is distinct from fully 'atomistic' molecular dynamics simulations, in which each constituent atom in several mineral sheets is modelled explicitly (e.g. Volkova et al., 2021; Zen et al., 2022).

Kaolinite is a layered material, consisting of alternating silica tetrahedral and alumina octahedral sheets. A single 'layer' consists of a tetrahedral silica sheet tightly-bonded via shared oxygen atoms to an alumina octahedral sheet. Each of these layers is around 0.72 *nm* thick (Mitchell and Soga, 2005). Kaolinite platelets have thicknesses in the region 10–100 *nm*, and so a typical kaolinite platelet contains at least several dozen of these repeating layers.

Each kaolinite platelet can be considered to have 3 distinct surfaces: two faces on opposite sides, and an edge surface consisting of exposed alternating sheets. To simulate the three distinct surfaces, the platelets are constructed from three different classes of spheres, as shown in Figure 1. The two largest surfaces (the two faces) consist of planar arrays of spheres, and the edge consists of a single row of spheres around the platelet perimeter. In these simulations, all platelets are constructed from 0.04 μm diameter spheres, and the platelets all have a thickness of 0.055 μm (a distribution of platelet diameters is used).

Due to the scale of kaolinite platelets, interactions are determined by the surface chemistry of the platelets and the surrounding fluid (Israelachvili, 2011) rather than by simple mechanical forces. Conventionally, it was assumed that the two external faces of kaolinite platelets were identical, both possessing a negative surface charge.

This was largely due to the difficulty in differentiating between the two face surfaces. In recent years however, thanks to the use of Atomic Force Microscopy (AFM), it is now established that due to the alternating sheets inherent in the platelets, the two faces of kaolinite platelets are chemically different—i.e. each platelet has one silica tetrahedral surface, and one alumina octahedral surface, and these two surfaces possess separate (and frequently opposite) surface charges. The silica tetrahedral face as well as the edge surface can be generally assumed to have permanent negative surface charges. In neutral-to-acidic conditions, the alumina face possesses a positive surface charge, whereas in alkaline conditions this face demonstrates an overall negative surface charge (e.g. Gupta et al., 2011; Liu et al., 2014b). Although this understanding is now well-established, the outdated view (of having two identical faces) has persisted somewhat in geotechnical engineering, which is reflected in the previous particle-scale simulations mentioned above, which didn't distinguish between the different platelet faces.

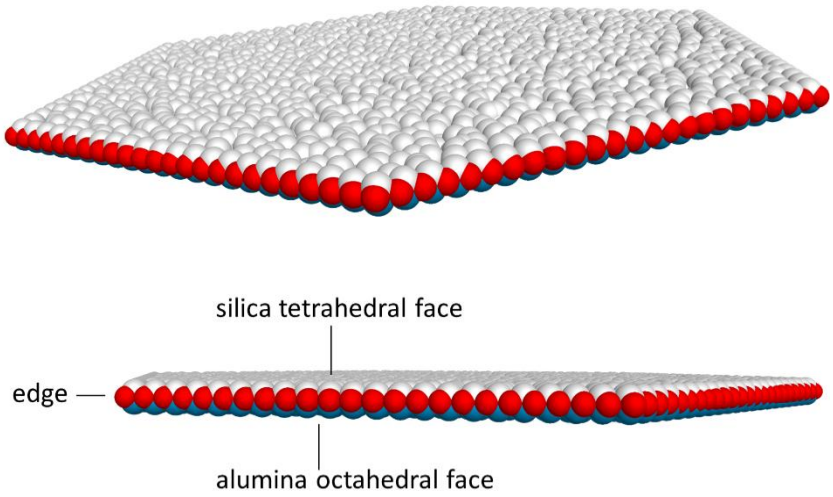

Figure 1. Platelets modelling using spheres in DEM. The platelet shown measures 1 μm in diameter, 0.055 μm in thickness and consists of 1238 spheres.

Interactions

It is necessary in DEM to define the interactions (force-distance functions) between the various platelet surfaces. This involves a significant degree of uncertainty, as it has not been possible to obtain any direct measurements of the forces between individual clay platelets. Indeed, it is essentially impossible to measure the forces between two flat surfaces—almost all surface force measurements are obtained using at least one curved surface (e.g. AFM).

In the previous studies of kaolinite (which did not consider the separate faces of each particle), other researchers have often defined the particle interactions based

on the classical Derjaguin-Landau-Verwey-Overbeek (DLVO) theory. The DLVO theory computes the force between like-charged particles, based on the interaction of their diffuse layers and van der Waals forces. This is problematic for two reasons: firstly, it does not allow for attraction between opposite-charged faces; and secondly, it is known that the DLVO theory often fails to accurately describe real particle behaviour (e.g. McBride and Baveye, 2002; Mitchell and Soga, 2005). This disparity can be attributed to the fact that the DLVO is a continuum theory, and gives no consideration to the discrete natures of the surfaces, fluid and ions (Alcantar et al., 2003; Israelachvili, 2011).

The simulations here assume an acidic environment (pH 5–6) with a moderate electrolyte content (0.01–0.1 mol/L), equivalent to both common soil conditions and to lab-prepared samples of kaolin without any adjustment (e.g. Wang and Siu, 2006). The different surface charges on kaolinite platelets are now well-established; and in most conditions, the silica face and edges are negatively charged, and the alumina face positively charged. In general, one can expect like-charged surfaces to demonstrate repulsion, and opposite-charged surfaces to demonstrate attraction (the two modes of behaviour shown in Figure 2). It is fairly straightforward to implement monotonically repulsive long-range interactions in DEM—provided that the stiffness at close-range is great enough to prevent any physical overlap, the only parameter that needs careful consideration is the range of interaction. Modelling attractive interactions between platelets involves more uncertainty, as this requires the magnitude of attraction forces to be defined (i.e. the 'pull off' force for platelets of given size).

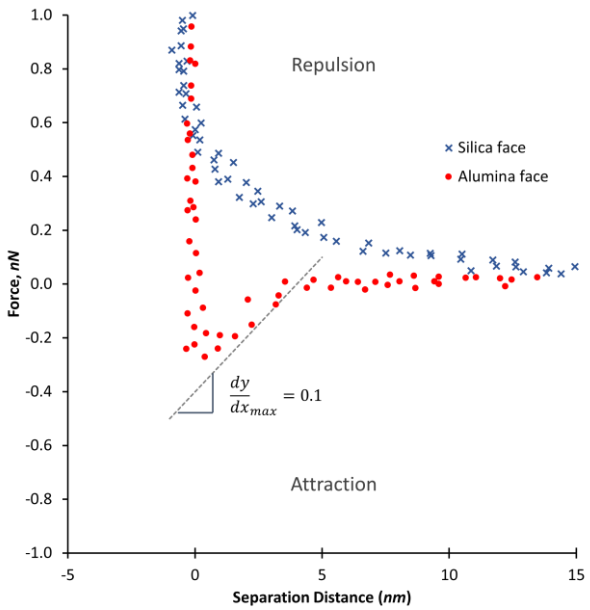

Figure 2. Typical AFM data from Gupta and Miller (2010); showing the interaction between a silicon tip and the two different faces of kaolinite platelets: pH = 6, tip radius = 120 nm, 1 mM KCl.

Figure 2 shows typical force-distance measurements obtained using AFM, reproduced from Gupta and Miller (2010), between a silicon tip and the two different faces of individual kaolinite particles. The two sets of points in this figure each consist of multiple readings from several particles, and clearly demonstrate the different surface charge on the two kaolinite faces. Using such experimental data, it is possible to qualitatively estimate the peak attractive (pull-off) forces between oppositely-charged kaolinite faces. As well as Gupta and Miller (2010), Liu et al. (2014a) and Kumar et al. (2016) also used AFM to measure force-distance functions between negatively-charged silicon tips and the positively-charged alumina-octahedral faces of individual kaolinite platelets. These three studies, using tips with radii of 120, 20, and 35 *nm* respectively, all reported pull-off forces of around 0.1–0.4 *nN* (e.g. 0.3 *nN* in Figure 2), at pHs 5–6 with moderate electrolyte contents. All three studies reported surface charge densities of the silicon tips that were very similar to those measured on the silica faces of kaolinite platelets. If one assumes that the tip material is representative of the kaolinite silica face, then one can estimate the force-distance relationship between equivalent flat surfaces using the useful Derjaguin approximation (Israelachvili, 2011):

$$E(D) = F(D)/2\pi R \qquad [1]$$

where $E(D)$ is the energy of interaction (per unit area) as a function of distance for two flat surfaces; $F(D)$ is the *measured* force-distance function for a rigid sphere interacting with a flat surface; and R is the radius of the sphere (in this case the tip). The force per unit area of interaction (i.e. the pressure) as a function of distance $P(D)$ can then be estimated by differentiating $E(D)$:

$$P(D) = -\frac{dE}{dD} = -\left(\frac{dF}{dD}\right)/2\pi R \qquad [2]$$

Estimating the maximum gradients from the data reported in Gupta and Miller (2010), Liu et al. (2014a), and Kumar et al. (2016), and dividing by ($2\pi R$), gives pull-off forces per unit area of between 100–500 *nN* / μm^2. The maximum gradient for the data in Figure 2 is labelled, and using a tip radius of 120 nm suggests a pull-off force (per area) of around 130 *nN* / μm^2. It is also worth noting that Israelachvili (2011) gives a typical pull-off force of 100 nN for colloidal (~1 μm) particles.

Based on the above estimates, as well as previous simulations by the authors which investigated varying adhesion forces (de Bono and McDowell, 2022b), a value of 100 *nN* / μm^2 was therefore chosen as the pull-off force between opposite-charged faces in this study, and the range of interaction was set at 0.010 μm. This

interaction is shown in Figure 3, alongside all other possible interactions between the kaolinite surfaces. Having defined the attractive silica-alumina surface interactions, repulsive interactions were then defined with similar close range stiffness and the same range of interaction, akin to the experimental data shown in Figure 2. For simplicity, both silica-silica and alumina-alumina face-to-face interactions are considered to be identical. Like the silica faces, the kaolinite edges are also negatively charged, but it is assumed here that the edges have a lower surface charge density than the silica faces, which means that the interaction forces *per unit area* are smaller for the edges (Figure 3). This is based on the fact that the edges consist of alternating layers of opposite charge, as well as from observations from previous simulations investigating flocculation (de Bono and McDowell, 2023) and AFM analysis of the edges (Gupta et al., 2011; Liu et al., 2014b). These interactions (as shown) implicitly include *all* colloidal forces between the surfaces (e.g. van der Waals, ion correlation forces, hydration forces etc.) (Israelachvili, 2011; van Olphen, 1963).

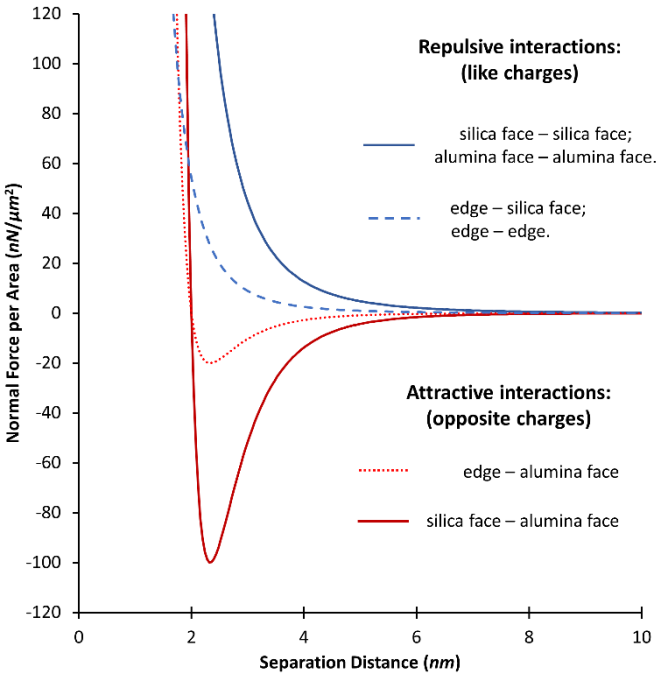

Figure 3. Platelet interactions between the various surfaces used in the DEM simulations

The interactions shown in Figure 3 are the net *platelet-to-platelet* interactions, which are the sum of many individual sphere-to-sphere interactions. In the DEM simulations, the interactions are computed between individual spheres, and so in order to achieve the specified platelet-to-platelet interactions, the *sphere-to-sphere* interactions must be calibrated. This process is done by adjusting the sphere-to-sphere interaction laws while measuring the net force-distance function between two platelet surfaces. Custom interaction laws are used for the sphere-to-sphere interactions, chosen solely to capture the shapes of the curves depicted in Figure 2 . These custom laws have the form:

$F \sim r^{-\alpha} - r^{-\beta}$ for the attractive case, similar to the well-known Lennard Jones equation; and $F \sim r^{-\alpha} + r^{-\beta}$ for repulsive interactions; where *F* is the normal force, *r* is the separation, and α, β are constants ($\alpha > \beta$). The parameters α, β as well as the constant of proportionality are adjusted such that the desired platelet interactions (those shown in Figure 3) are obtained, and will depend on the density of spheres in each platelet. A more detailed explanation, demonstrating how to calibrate *any* desired platelet interaction can be found in de Bono and McDowell (2022a). It should be noted that in the previous studies (e.g. Sjoblom, 2015) which have used spheres to model kaolinite platelets (the same approach used here), those authors have assumed or implied that the net platelet interactions are simply the sphere-to-sphere interactions scaled by the number of interacting spheres. However, the surface separation between two interacting spheres will almost certainly not equal the surface separation between the two platelets—a problem exacerbated by the fact that these earlier studies frequently used lattice arrangements of spheres. It is essential that the sphere-to-sphere interactions are calibrated in order to achieve the desired platelet-to-platelet behaviour, and furthermore, to ensure repeatability it is important that the spheres are given random internal displacements within each platelet to avoid any interlocking effect (de Bono and McDowell, 2022a).

Tangential platelet interactions are implemented using a simple linear tangential stiffness with a coefficient of friction. It is known that adhesion has a significant effect on the measured friction forces between molecularly smooth materials (e.g. Gao et al., 2004; Israelachvili, 2011). For example, it has been shown that mica, which is smooth and chemically similar to the silica face of kaolinite, under a given normal load, can demonstrate friction forces 100 times greater when sliding in adhesive contact compared to purely repulsive contact (Homola et al., 1990, 1989). For reasons that will be shown later in this paper, it was found that modelling such adhesion-dependent friction was essential for reproducing realistic bulk behaviour of the samples. As such, in these simulations, a coefficient of friction of 1.0 is used for attractive (adhesive) face-to-face interactions, and a low coefficient of friction of 0.01 is used for repulsive (non-adhesive) face-to-face interactions. For all other interactions, involving kaolinite edges, a coefficient of 0.2 is used. Although this modelling approach enables the correct behaviour to be achieved, it should be emphasised that these values were chosen arbitrarily and are very much a simplification (suitable for such a coarse-grained simulation). Although a coefficient of friction of around 0.01–0.05 for smooth surfaces in repulsive contact is reasonable, as is the value of 0.2 for the 'non-smooth' edges—it is known that the friction force for adhesive contacts is not linearly proportional to the normal load (e.g. Gao et al., 2004; Israelachvili, 2011). For adhesive contacts at this

scale, although the friction force increases with load, it usually increases linearly with the 'true' contact area (and will additionally depend on the nature of the counterions).

For simplicity, and to minimise the input variables in the simulations, the boundaries are considered identical to the silica faces of kaolinite platelets. That is, any platelet surface interacting with a boundary experiences the same interaction (per unit area) as it would with a silica surface of a platelet; with the difference being no friction forces act with the boundaries to reduce any potential boundary effects. All interactions have a 'cut off' range of 10 *nm*, meaning no interactions exist or are active beyond this range. A summary of all defined interactions are given in Table 1.

Table 1. Summary details of interactions between platelet surfaces.

Interacting Surfaces		**Type**	**Pull-off Force ($nN/\mu m^2$)**	**Interaction Range (nm)**	**Friction Coefficient, μ**
silica face	alumina face	*attractive*	100	10	1.0
silica face	silica face	*repulsive*	0	10	0.01
alumina face	alumina face	*repulsive*	0	10	0.01
silica face	edge	*repulsive*	0	10	0.2
alumina face	edge	*attractive*	20	10	0.2
edge	edge	*repulsive*	0	10	0.2
silica face	boundary	*repulsive*	0	10	0.0
alumina face	boundary	*attractive*	100	10	0.0
edge	boundary	*repulsive*	0	10	0.0

Simulation Procedure

The aim of these simulations was to capture key features of soil behaviour, especially those which have not yet been achieved for clays, such as dilative and contractive shearing to critical states. To do this, it was chosen to first isotropically compress a cylindrical sample using a deformable membrane. The use of a membrane (as opposed to a rigid box), ensures a uniform radial pressure is applied, and allows samples to deform naturally. The samples are then sheared in triaxial conditions directly following isotropic compression. Three different triaxial loading paths are simulated: constant confining pressure (σ_3), constant mean stress (p), and constant volume. The software used for the simulations was Itasca's PFC3D v6.0 (Itasca, 2015), on an Intel 18-Core CPU (Xeon W-2195) with 128 GB RAM.

To create the sample, platelets are randomly generated in a cylinder 6 μm in diameter and 20 μm in height, at a bulk porosity of 0.75. This results in 4080 platelets, comprising three different sizes: diameters of 1.5, 1.0 and 0.75 μm. Each platelet size

fraction constitutes an equal proportion by mass of the sample (so there are more smaller platelets). All platelets have the same thickness (0.055 μm), giving realistic platelet aspect ratios of 27, 18, and 14. 4080 platelets is obviously a small quantity for a sample of clay, and is unlikely to achieve a true representative element volume (REV). When modelling kaolinite using discs, Bandera et al. (2021) suggested 1000 platelets is too few, whilst 10000 appeared enough to achieve an REV capable of inferring information about the bulk material. Modelling 4080 platelets here requires the use of approximately 5,000,000 spheres, which was considered the limit for these investigative simulations on the available hardware. It should be noted that in terms of the number of platelets and their aspect ratio, this study goes beyond the previous studies using the multiple-sphere method to model platelets. The typical timestep in the simulations was of the order 1×10^{-11} sec, and equilibrium was judged to have been reached when the sample(s) reached an approximately static state, with minimal particle velocities.

After being created, the platelets in the sparse initial sample are allowed to come to equilibrium under gravity. The sample is then compacted by applying a vertical load to the top wall, the purpose of which is to create a denser sample, with an aspect ratio and initial voids ratio suitable for isotropic compression and subsequent triaxial shearing. In this particular case, a vertical load of 120 kPa was suitable to achieve a voids ratio of around 1.6 and an aspect ratio of approximately 2:1, which was taken as the starting point for all subsequent simulations. After this compaction, the sample is unloaded and then enclosed in a faceted, deformable membrane, and the sample is then allowed to come to equilibrium again. This method was followed primarily to achieve a sample suitable for the isotropic and triaxial loading.

The membrane consists of rigid triangular facets, with each facet sharing vertices (the 3 corner points) with neighbouring facets. It is the same membrane and triaxial model as used previously by the authors when modelling coarse granular soils (see images and description in de Bono and McDowell, 2017). For the isotropic compression simulations, the radial membrane is used to apply a uniform confining pressure via a servo-control, which moves each individual vertex inwards or outwards depending on the difference between the desired target stress, and the stress measured on the surrounding facets. The velocity of each vertex is proportional to this difference, and is set to zero when the stress is within a small tolerance of the target. The top (planar) wall is controlled in a similar way, but moved as a rigid body, to apply the desired vertical stress to the sample. During the triaxial tests, the top wall is used to apply axial strain increments instead of a load, while the membrane is used to either: maintain a constant confining

pressure, maintain a constant mean stress, or maintain a constant volume; depending on the type of triaxial test.

RESULTS

Normal Compression

The isotropic normal compression behaviour is shown in Figure 4(a), with an image of the compressed sample at 1 MPa in (b). The material displays a clear yielding at around 100 kPa, evident by increased rate of volumetric compression and a change in gradient of the compression curve. This yielding is followed by a normal compression line which is linear when voids ratio is plotted against log-stress. If the normal compression line is defined by:

$$e = e_0 - C_C \log p \qquad [1]$$

where e_0 is the voids ratio at some reference value of p (e.g. 1 kPa), then the simulation gives a compressibility of C_c = 0.120. This is lower than typical values for kaolin (0.2–0.3, Hattab, 2011), but of interest here is the ability of the material to undergo irreversible volumetric compression, and the existence of a linear normal compression line in e –log p space. Upon unloading, the sample reveals a non-linear swelling line, with an increasing slope as stress reduces, reminiscent of real clays (Al-Tabbaa, 1987; Burland, 1990; Wood, 1990). Approximating the unloading path with a straight line, gives a slope of C_s = 0.055, and a ratio between C_c / C_s of 2.2, consistent with experimental data (e.g. Hattab and Hicher, 2004, where $C_c/C_s \sim 3$).

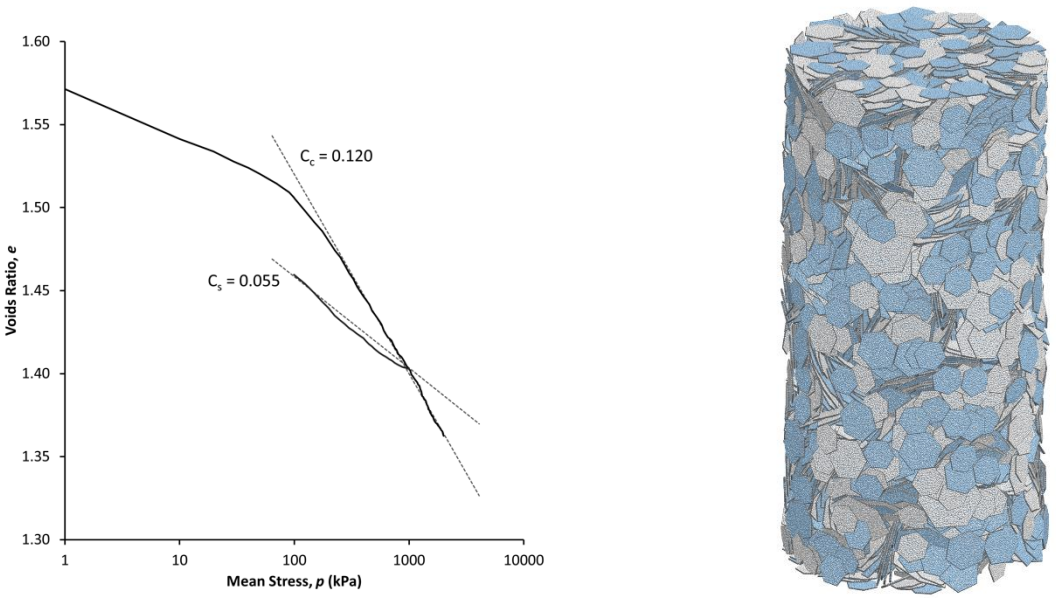

(a) (b)

Figure 4. Isotropic normal compression results (a); and image of the virtual sample after compression to 1 MPa (b). The two colours in the image indicate the different faces of kaolinite particles.

An interesting outcome of this work is it was found that in order to achieve both realistic compression and shearing behaviour, it is essential that the coefficient of friction between two platelets varies depending on which two surfaces are interacting (as described earlier). Given the general lack of experimental data on the frictional behaviour between kaolinite platelets, initial trial simulations used a single coefficient of friction for all surface interactions. It was quickly established that a low value (as one might expect for smooth platelets), was required to achieve realistic normal compression lines—using a large value of friction would lead to curved, quasi-elastic compression curves, shown by the upper curve in Figure 5. However, a uniform low coefficient of friction results in a very low shear strength, leading to liquefaction during triaxial simulations. This spurred the use of adhesion-dependent friction, an approach supported by experimental observations on mica (chemically similar to the silica face of kaolinite, but available in large sheets), which exhibits much higher friction forces between adhesive surfaces compared to repulsive surfaces (Homola et al., 1990, 1989).

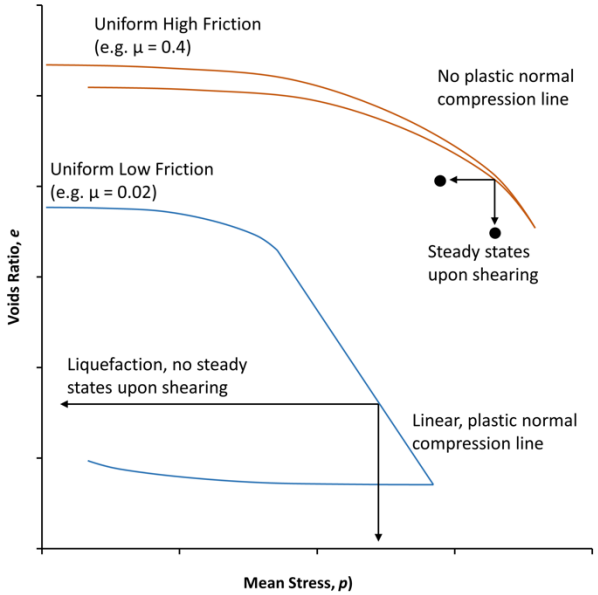

Figure 5. Diagram showing behaviour when using uniform coefficient of friction for all platelet interactions.

As no individual breakage of platelets occurs in these simulations, the irreversible compression can only be due to rearrangement of platelets into a denser packing. The compressibility (i.e. the slope of the normal compression line) appears to be influenced by the platelet interactions (and is particularly sensitive to the inter-platelet friction). The densification of the sample during isotropic compression is caused by a rearrangement of platelets, and this change is reflected in the many measurements possible in DEM. Figure 6(a) shows the particle orientations with respect to the horizontal plane at isotropic stresses of 100 and 2000 kPa. This is calculated as the angle between the platelets and the horizontal plane (e.g. 90° indicates a platelet aligned vertically). This plot shows that despite the volume change, there is little distortion to the platelet fabric, which remains fairly isotropic (in contrast to results shown later). Figure 6(b) shows the number of interactions (or 'contacts') as well as the 'exposed' free surface area of the platelets throughout compression. The number of interactions increases monotonically during the test, with a marked change in rate of increase at around 100 kPa, corresponding to the approximate yield stress in Figure 4(a). The free surface area of the platelets, defined as the surface area of platelets which has no interactions with any neighbouring platelets, also decreases as the sample undergoes volumetric compression. Again, an apparent change is visible around the yield stress of 100 kPa, after which the available surface area decreases slightly more rapidly.

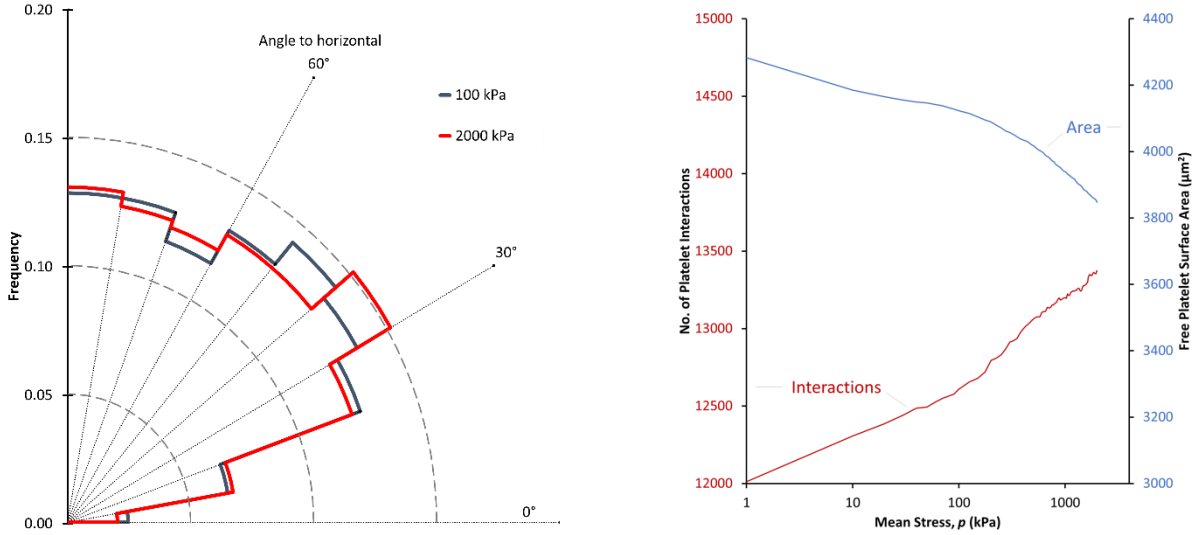

(a) (b)

Figure 6. Radial histogram showing frequencies of platelet orientations with respect to the horizontal (a); and graph showing the number of interactions and free surface area of the platelets during compression (b).

The interactions between platelets can be notionally categorised into face-to-face, edge-to-face and edge-to-edge (e.g. O'Brien, 1971; van Olphen, 1963) (not considering interactions with the boundaries). Figure 7(a) shows the overall number of contacts as a function of stress, classified into these 3 types. The clear majority of contacts appear to be edge-to-face, although these quantities are slightly sensitive to the criteria used to classify the interactions. The majority of interactions involve spheres on both the faces and edges of platelets (see Figure 1). Face-to-face interactions are defined as those in which the two platelets are approximately parallel (±2°), and have a clearly defined 'contact area'. Edge-to-edge interactions are identified as those in which only the edge spheres are interacting. All other contacts are classified as edge-to-face contacts; this method of classification was confirmed visually. The main contributor to the increasing number of interactions (or 'contacts') is edge-to-face interactions. Figure 7(b) shows the total area of 'contact' between platelets, broken down into the types of interaction. Despite face-to-face interactions being the least common mode of interaction between platelets, they unsurprisingly represent the largest area of interaction. However as the sample undergoes volumetric compression, the increase in contact area is due to the increase in edge-to-face contacts.

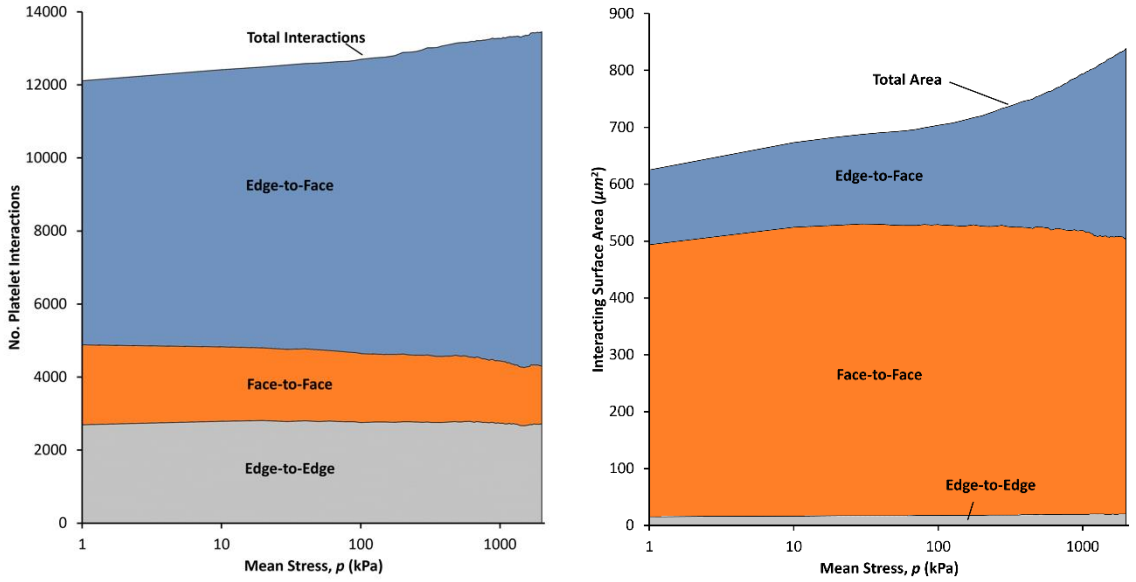

(a) (b)

Figure 7. Graphs showing quantities of different platelet interactions against stress (a); area of 'contact' between platelets according to mode of interaction (b).

As shown in Figure 7(a), the number of face-to-face interactions slightly decreases during compression. These face-to-face interactions are approximately equally split between adhesive and repulsive interactions (i.e., between like or opposite charged faces). It is well known that kaolinite platelets readily aggregate into 'stacks' (e.g. Du et al., 2009; Ma and Pierre, 1999). Most aggregation occurs during the virgin compression of the initial loose sample at high voids ratio (de Bono and McDowell, 2022b), meaning a distribution of stacks exists prior to the isotropic compression. In this case, 'stacked' platelets are identified as platelets which are in face-to-face contact, and the surface separation is less than or equal to 0.002 μm (see Figure 3). Figure 8(a) shows the number of such 'stacked' interactions throughout the compression test, subdivided according to the two surfaces interacting. At the start of compression, one can see that only attractive, oppositely-charged faces are in close face-to-face contact. However, as the applied stress increases, repulsive faces are also forced together into a 'stacked' arrangement (although these platelets would separate upon unloading). Figure 8(b) shows the stack size distribution before and after compression, where a stack is defined as a group of platelets stacked together in *adhesive* face-to-face arrangement. One can see that there are fewer adhesive stacks existing after compression (and more free platelets), indicative of breakage or degradation of stacks during compression.

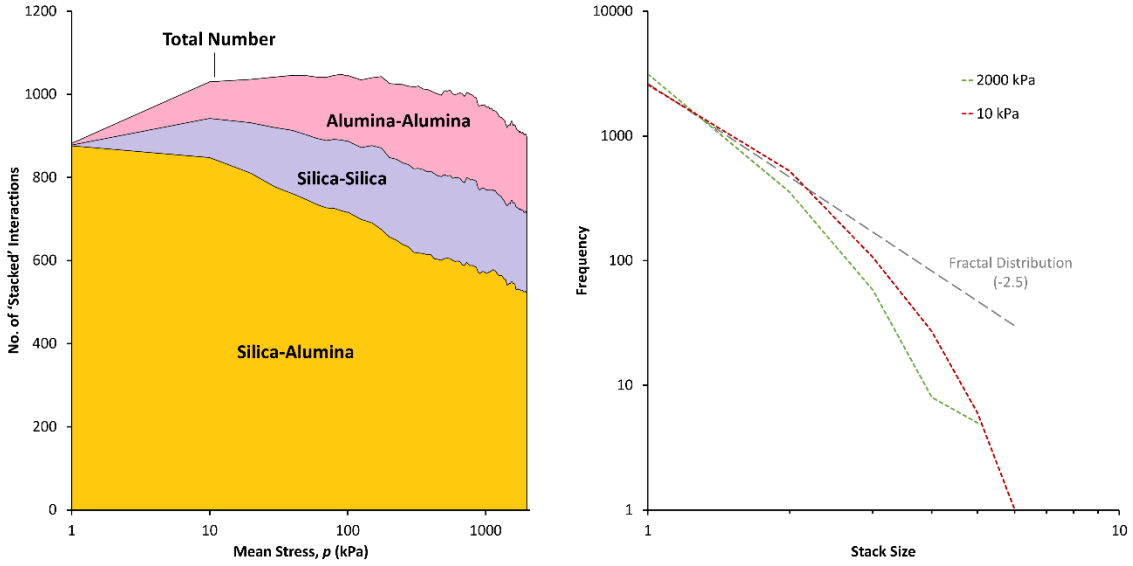

Figure 8. Total Number of 'stacked' close face-to-face interactions (a); stack size distribution (b).

Figure 9 shows the average platelet coordination number plotted against applied stress. The coordination number represents how many neighbouring platelets any individual platelet is interacting with, and shows a monotonic increase as one would expect. For coarse-grained, crushable soils, a unique constant coordination number has been observed on the normal compression line(de Bono and McDowell, 2018)—where increasing contacts are balanced by an increasing number of new fine particles. In this case, there is no crushing of platelets, and so the average platelet coordination number increases as the platelets move into a denser packing and interact with more neighbouring platelets. In terms of space-filling, stacks of platelets (regardless of adhesion) may effectively be considered as single entities or 'macro particles', as there is no significant void space between them. With this in mind, also plotted in Figure 9 is the average coordination number per 'body', which considers all stacks as single particles. In this case, the average coordination number appears to plateau and approach a constant value, although this occurs quite some time after yielding, and appears to coincide with when the total number of stacks decreases. Unfortunately, the relatively small sample sizes limits the data here; it is possible that with a significantly larger sample, there could be a continued increase in repulsive face-to-face contacts (cf. Figure 8).

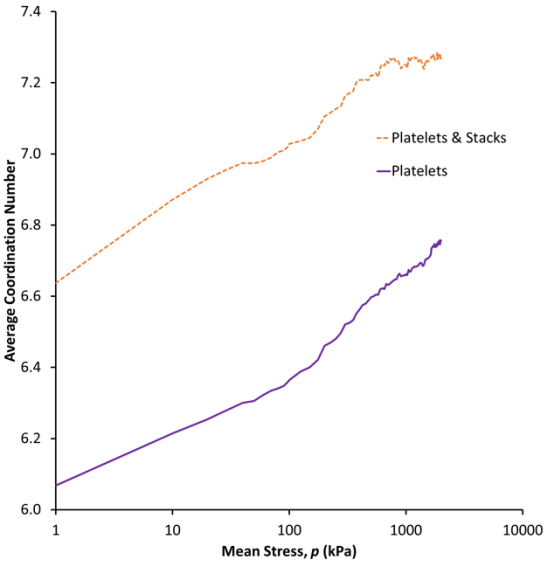

Figure 9. Average coordination plotted against mean stress p.

Triaxial Shearing

A range of triaxial tests were performed from normally consolidated (NC) and overconsolidated (OC) states, including constant-σ_3, constant-p and constant-volume tests. The NC tests were performed from isotropic states of 100 and 200 kPa, and the OC tests were performed from an isotropic of 100 kPa having been unloaded from 1000 kPa (OCR=10). The tests were stopped after reaching steady states with no major changes in stresses and volume, and the final states were assumed to be critical states. This decision, as well as the relatively small number of triaxial tests, was due to the large computational time required for each simulation (several weeks for a single test). The deviatoric stress-strain results for the constant-σ_3 and constant-p tests are shown in Figure 10, along with the volumetric responses.

Figure 11 shows the stress paths for the 'undrained' constant-volume tests, as well as the critical states from all tests. The critical states reveal a well-defined critical state line in q-p space with M = 0.60, which compares to $M \approx 1$ for real kaolin (e.g. Hattab, 2011). This value of M = 0.60 is equivalent to a critical state friction angle of 15°, which although on the low side, is not inconsistent with values expected for clays. These constant-volume exhibit stress paths consistent with real clays (e.g. Anandarajah and Zhao, 2000; Hattab and Hicher, 2004; Wroth, 1987), with a clear difference between the normal and overconsolidated samples sheared from p = 100 kPa.

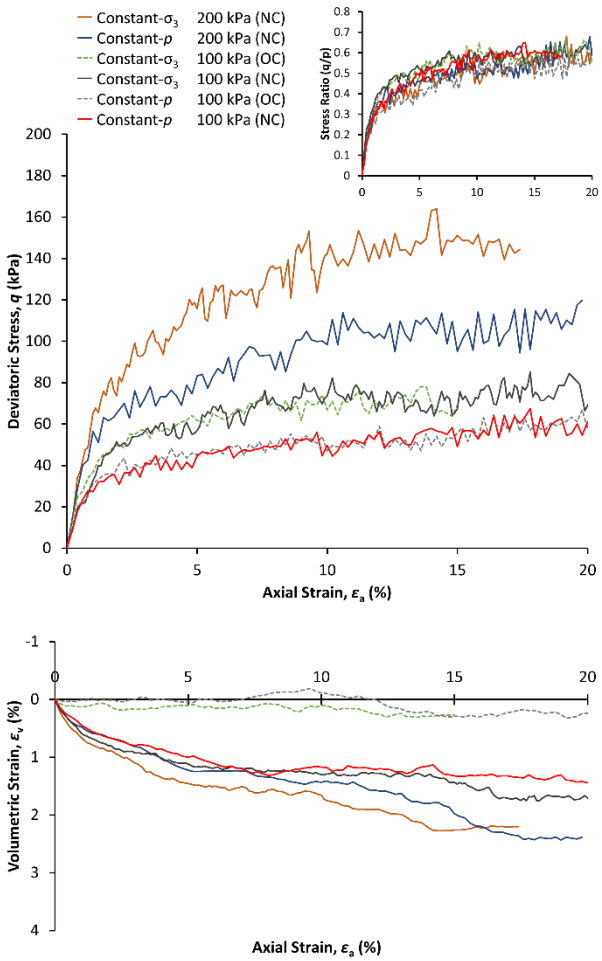

Figure 10. Triaxial results showing deviatoric (above) and volumetric (below) responses from the constant-σ_3 and constant-p tests. The inset shows the stress ratio (q/p).

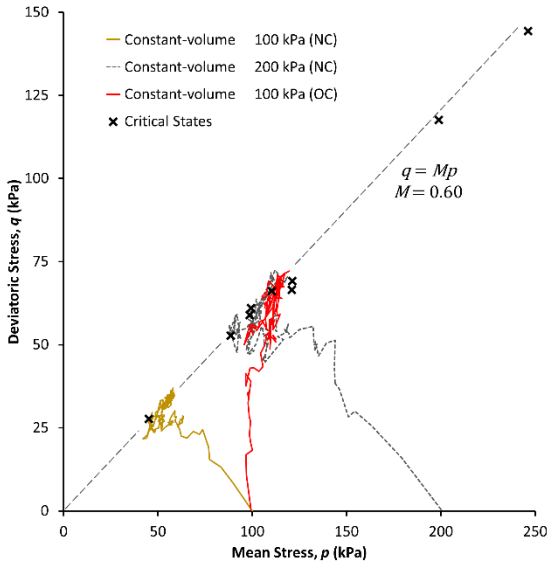

Figure 11. Stress paths for the constant volume triaxials tests, as well as critical states plotted in q-p space.

The critical states are plotted in Figure 12(a) in terms of voids ratio and mean stress, with the initial states and paths also shown. The overconsolidated samples show mildly

dilative behaviour, with the constant-p test displaying no overall change in volume. For real kaolin, one would expect much more dilative behaviour at an OCR of 10 (see Hattab and Hicher, 2004)—which should be possible to achieve with further refinement of the model (particularly concerning the tangential behaviour between the different platelet surfaces). Figure 12(b) shows the critical states together with an apparent critical state line, which is parallel to the normal compression line in agreement with experimental data. The isotropic normal compression line and critical state line have a horizontal separation (on the log stress scale) of a factor of 3—this compares to a typical factor of 2 obtained for real kaolin (Hattab and Hicher, 2004).

The only other attempt to simulate shearing of clays using DEM (Aminpour and Sjoblom, 2019) recorded stress ratios of $\eta \leq 0.4$ at axial strains of 20% in constant-σ_3 tests, and did not report any critical states (and/or volumetric behaviour). It is worth noting again that it was found that using a uniform, low coefficient of friction for all platelet interactions leads to liquefaction in constant-volume tests (and no ultimate steady volume in the constant-σ_3 and constant-p tests). So the work presented here appears to be the first particle-scale model of clay able to reproduce qualitatively correct normal compression and triaxial shearing behaviour.

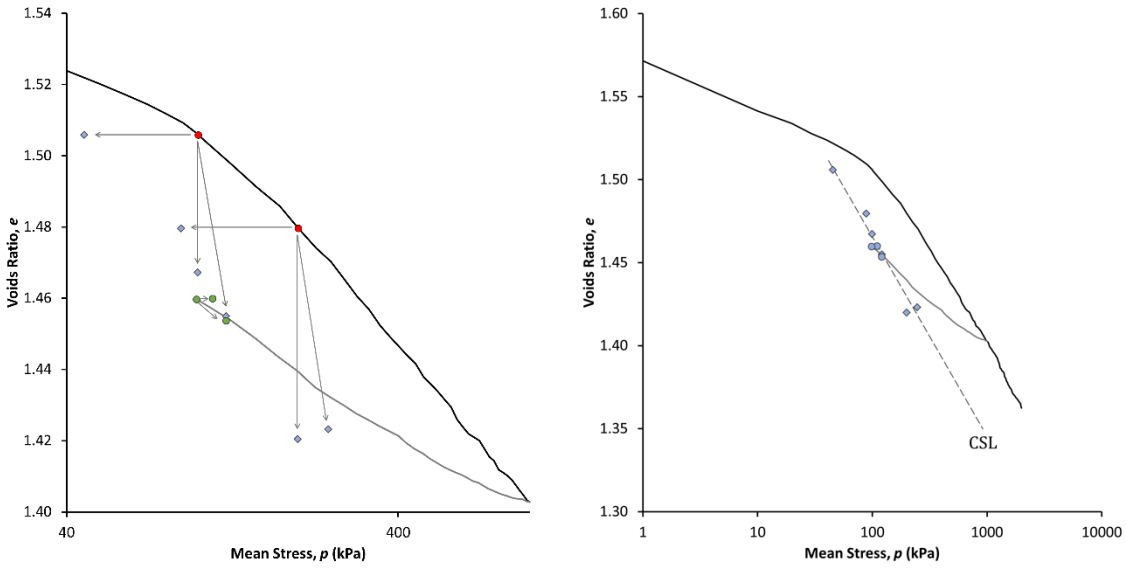

(a) (d)

Figure 12. Voids ratio versus mean stress plots showing critical states and stress paths (a), and estimated critical state line (b).

Given the slope of the unloading path (C_s) in Figure 4(a), it is possible to estimate the *current* preconsolidation pressure (p_0) at any point during the triaxial tests. This is done by projecting a linear unload/reload line from the current state (e, p) and calculating the intersection with the isotropic normal compression line. Normalising the deviatoric and mean stresses by this current preconsolidation pressure allows normalised stress paths

to be plotted, as shown in Figure 13(a), which suggest a state boundary surface reminiscent of real data for clays (e.g. Cotecchia and Chandler, 2000; Westerberg, 1995).

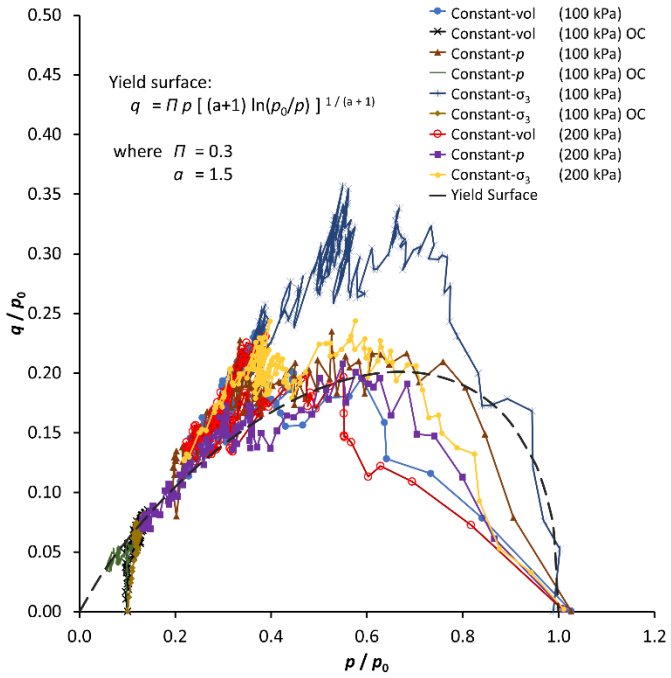

Figure 13. State boundary surface obtained by normalising the stress paths by the estimated preconsolidation pressure.

In the classical critical state framework, normal compressions lines are often defined in the compression plane in terms of specific volume v, and using natural logarithms:

$$v = N - \lambda \ln p \qquad [4]$$

where N is the value of v on the projected linear normal compression at a mean stress of p = 1 kPa, and λ is the slope (and so λ = C_c / 2.3). Any parallel line can be described similarly, with a different intercept (N). If the critical state line is described by:

$$v = \Gamma - \lambda \ln p \qquad [5]$$

and if the slope of the unload/reload line is κ, then:

$$N - \Gamma = (\lambda - \kappa) \ln(p_0/p_c) \qquad [6]$$

where p_0 is the isotropic preconsolidation pressure, and p_c is the value of mean stress at the critical state along the unload line. Based on the normal compression and critical state lines (Figure 12b) and solving Eq. [6] it seems for this material that:

$$\ln(p_0/p_c) \approx 2.2 \qquad [7]$$

which is consistent with the OC triaxial results, for example the constant volume test at an OCR of 10 has a critical state close to the initial value of p ($\ln(10) = 2.3$).

According to McDowell (2002, 2000), a simple family of yield curves based on micro mechanics is given by:

$$q = \Pi p[(1 + a) \ln(p_0/p)]^{1/(1+a)} \qquad [8]$$

where Π is the stress ratio at the apex of the yield surface (peak q), and the flow-rule can be non-associative. For this material, using a value of M = 0.6 (with $p = p_c$), and Π = 0.3, which describes the majority of the data in Figure 13 well, solving Eq. [8] using $\ln(p_0/p_c) \approx 2.2$ gives a value of a = 1.5, and allows a state boundary surface to be conjectured and is drawn in Figure 13. This is not to propose a specific yield surface, and the failure on the dry side of critical states clearly exhibits Hvorslev-like behaviour, but intends to give the reader confidence that the numerical clay is exhibiting behaviour that is consistent with our well established notion of an existing critical state framework.

Analysis of the particle-scale behaviour during the triaxial tests reveals a contrast to the observations from normal compression. During the course of all shear tests, there is a decrease in the overall number of platelet interactions, despite most (drained) tests undergoing volumetric contraction. This reflects observations made from previous studies investigating coarse soils, which found lower average coordination numbers on the critical state line compared to the normal compression line (de Bono and McDowell, 2018). To highlight these trends, Figure 14 shows details from the NC constant-p triaxial test from p = 100 kPa. Figure 14(a) shows the macroscopic behaviour, including the volumetric response. Figure 14(b) shows the number of interactions, number of face-to-face interactions and the free surface area of the platelets against axial strain. The results in Figure 14(b) are typical of all tests, and reveal that although the overall number of interactions reduces with shear strain, the number of face-to-face interactions actually increases slightly. The overall reduction in interactions is primarily due to a loss of edge-to-face interactions. Given the constant number of platelets, the total number of interactions corresponds directly to the average coordination number—which therefore also decreases. Interestingly, despite this reduction in platelet interactions, the available free surface area of the platelets actually decreases slightly, due to the increase in face-to-face contacts. Although not shown, the number of 'stacks' stays approximately constant or very slightly increases throughout the shear tests.

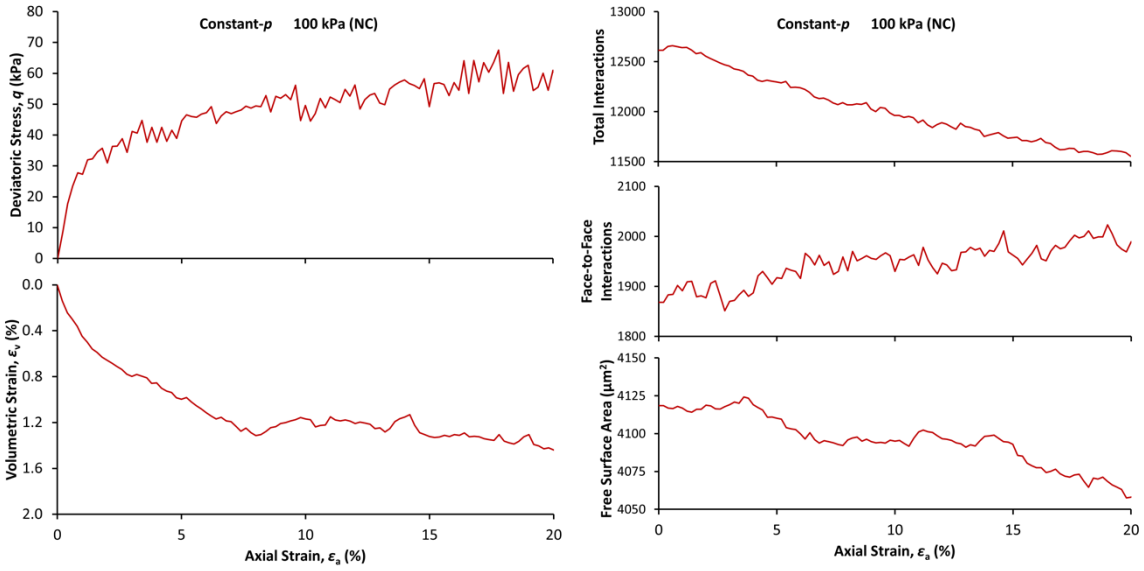

(a) (b)

Figure 14. Triaxial results from the constant-p test from p=100 kPa (a), changes in the number of interactions and free surface area as functions of axial strain (b).

Figure 15 shows the distribution of platelet orientations with respect to the horizontal plane before and after shearing. In contrast to normal compression (Figure 6), shearing induces a change to the 'fabric' of the platelets, which becomes more anisotropic—there appears to be a preferential orientation of platelets between 10—40° to the horizontal. Figure 16 shows internal cross sections of the samples on a vertical plane, before and after shearing. The shading corresponds to their orientation with respect to the horizontal, and one can observe a greater mix of random orientations before shearing, and a more horizontal alignment of platelets afterwards.

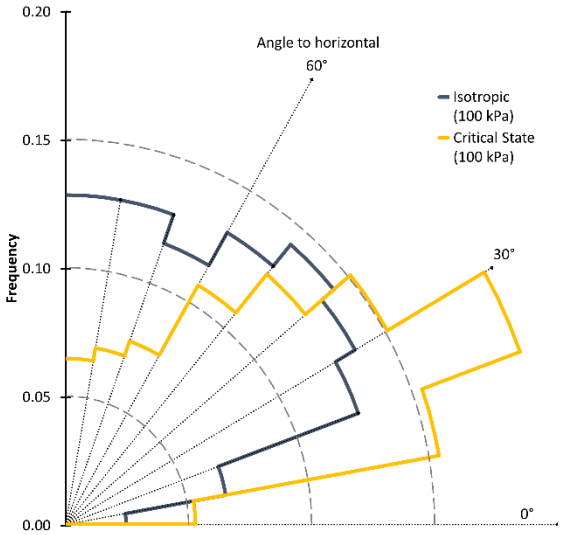

Figure 15. Radial histogram showing platelet orientations before and after shearing.

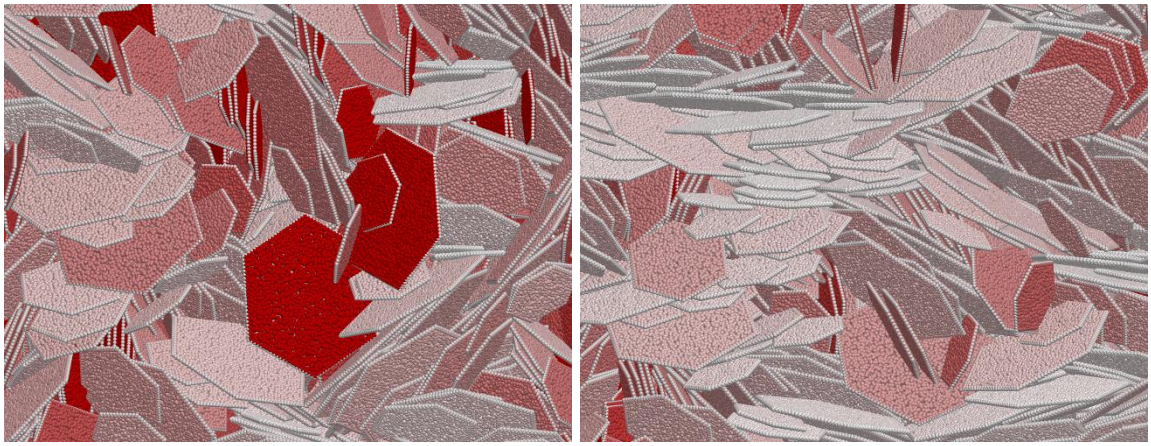

(a) (b)

Figure 16. Cross sections showing internal platelet orientations before (a) and after (b) shearing at p=100 kPa. Darker red indicates more vertical orientation, white indicates horizontal orientation.

Figure 17 shows the average platelet coordination numbers measured at the critical states. Similar to during normal compression, it appears there is a relation between average coordination number and mean stress on the critical state line.

Past work investigating the micro mechanics of (crushable) soils has related particle-scale properties to the macroscopic voids ratio (de Bono and McDowell, 2020). Figure 18 shows one such particle-scale measurement—the median edge-to-face separation—plotted against the macroscopic voids ratio. For platelets interacting edge-to-face, this separation is measured as the surface separation between the centre of mass of one platelet and the plane of the other, as shown in the figure. The data is plotted for both normal compression and critical states, and for both cases suggests a direct proportionality (note that the axes do not include the origin). Although the data is limited, this simplistic measure shows promise in leading to some insights to how particle-scale properties control the macroscopic properties, for example it is hoped that eventually DEM simulations will lead to a theoretical explanation of how the particle packing controls the macroscopic physical properties such as the porosity or permeability, as has been done for sands.

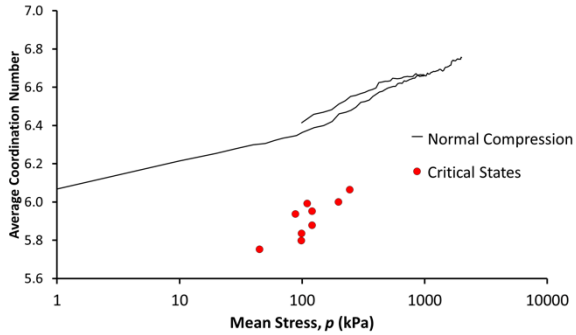

Figure 17. Average coordination number against mean stress during compression and at critical states.

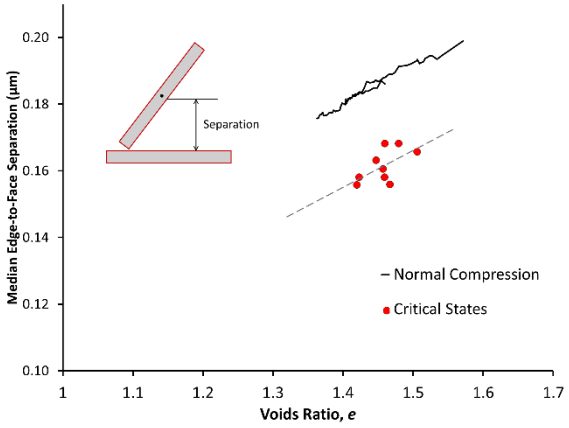

Figure 18. Median edge-to-face separation plotted against voids ratio for normal compression and critical states.

CONCLUSIONS

This work has demonstrated, for the first time, particle-scale simulations of clay capable of reproducing qualitatively correct compression and shearing behaviour. By modelling platelets with multifaceted interactions (which take into account the different properties of the platelet surfaces), it was possible to obtain a normal compression line and then shear a range of samples to critical states. It was found that in order to obtain a linear and plastic normal compression line in *e*-log *p* space whilst avoiding liquefaction or excessive contraction in the subsequent shear tests, it was necessary to implement different frictional behaviour between adhesive and repulsive interactions between the platelets. This enabled a critical state line to be established, which is a significant achievement for particle-scale simulations of clays. The simulations here go beyond all previous studies in terms of accurate interactions and the observed macroscopic behaviour. Analysis of the compression and shearing simulations revealed several interesting insights to the micro-scale behaviour, such as how the modes of platelet interactions change during compression and shearing, and a correlation between platelet separation and the bulk voids ratio.

The simulations presented here show that it is now possible to reproduce the most important and fundamental components of bulk clay behaviour using a particle-scale approach. This should help pave the way for further high-fidelity studies that are able to uncover the origins of the many little-understood features of clay behaviour (for example, hysteresis, or strain-rate effects. The key findings here—considering each individual platelet surface, and implementing surface-specific friction—are applicable to all clay minerals (in addition to the kaolinite simulated here).

To further enhance the computational modelling of clays, there remains a need for more specific particle-level experimental data. For example, measurements of normal (as well as tangential) force-distance interactions been *two clay surfaces* (conceivably by use of advanced colloidal probes) would greatly aid in understanding and modelling the interactions between such particles.

Acknowledgements

This work was supported by the Engineering and Physical Sciences Research Council [grant number EP/S016228/1].

Al-Tabbaa, A., 1987. Permeability and stress-strain response of speswhite kaolin. Cambridge University.
Alcantar, N., Israelachvili, J., Boles, J., 2003. Forces and ionic transport between mica surfaces: Implications for pressure solution. Geochim. Cosmochim. Acta 67, 1289–1304. https://doi.org/10.1016/S0016-7037(02)01270-X
Aminpour, P., Sjoblom, K.J., 2019. Multi-scale modelling of kaolinite triaxial behaviour. Géotechnique Lett. 9, 178–185. https://doi.org/10.1680/jgele.18.00194
Anandarajah, A., 2000. Numerical simulation of one-dimensional behaviour of a kaolinite. Geotechnique 50, 509–519. https://doi.org/10.1680/geot.2000.50.5.509
Anandarajah, A., Zhao, D., 2000. Triaxial Behavior of Kaolinite in Different Pore Fluids. J. Geotech. Geoenvironmental Eng. 126, 148–156. https://doi.org/10.1061/(ASCE)1090-0241(2000)126:2(148)
Bandera, S., O'Sullivan, C., Tangney, P., Angioletti-Uberti, S., 2021. Coarse-grained molecular dynamics simulations of clay compression. Comput. Geotech. 138, 104333. https://doi.org/10.1016/j.compgeo.2021.104333
Bayesteh, H., Hoseini, A., 2021. Effect of mechanical and electro-chemical contacts on the particle orientation of clay minerals during swelling and sedimentation: A DEM simulation. Comput. Geotech. 130, 103913. https://doi.org/10.1016/j.compgeo.2020.103913
Bayesteh, H., Mirghasemi, A.A., 2013. Procedure to detect the contact of platy cohesive particles in discrete element analysis. Powder Technol. 244, 75–84. https://doi.org/10.1016/j.powtec.2013.04.001
Burland, J.B., 1990. On the compressibility and shear strength of natural clays. Géotechnique 40, 329–378. https://doi.org/10.1680/geot.1990.40.3.329
Cotecchia, F., Chandler, R.J., 2000. A general framework for the mechanical behaviour of clays. Géotechnique 50, 431–447. https://doi.org/10.1680/geot.2000.50.4.431
de Bono, J.P., McDowell, G.R., 2023. Simulating multifaceted interactions between kaolinite platelets. Powder Technol. 413, 118062. https://doi.org/10.1016/j.powtec.2022.118062
de Bono, J.P., McDowell, G.R., 2022a. Some important aspects of modelling clay platelet interactions using DEM. Powder Technol. 398, 117056. https://doi.org/10.1016/j.powtec.2021.117056
de Bono, J.P., McDowell, G.R., 2022b. Discrete element modelling of normal compression of clay. J. Mech. Phys. Solids 162, 104847. https://doi.org/10.1016/j.jmps.2022.104847
de Bono, J.P., McDowell, G.R., 2020. On the packing and crushing of granular materials. Int. J. Solids Struct. 187, 133–140. https://doi.org/10.1016/j.ijsolstr.2018.07.011
de Bono, J.P., McDowell, G.R., 2018. Micro mechanics of the critical state line at high stresses. Comput. Geotech. 98, 181–188. https://doi.org/10.1016/j.compgeo.2018.02.016
de Bono, J.P., McDowell, G.R., 2017. Micro mechanics of drained and undrained shearing of compacted and overconsolidated crushable sand. Géotechnique 68, 1–15. https://doi.org/10.1680/jgeot.16.P.318
Du, J., Pushkarova, R.A., Smart, R.S.C., 2009. A cryo-SEM study of aggregate and floc structure changes during clay settling and raking processes. Int. J. Miner. Process. 93, 66–72. https://doi.org/10.1016/j.minpro.2009.06.004
Ebrahimi, D., Pellenq, R.J.-M., Whittle, A.J., 2016. Mesoscale simulation of clay aggregate formation and mechanical properties. Granul. Matter 18, 49. https://doi.org/10.1007/s10035-016-0655-8
Gao, J., Luedtke, W.D., Gourdon, D., Ruths, M., Israelachvili, J.N., Landman, U., 2004. Frictional Forces and Amontons' Law: From the Molecular to the Macroscopic Scale. J. Phys. Chem. B 108, 3410–3425. https://doi.org/10.1021/jp036362l
Guo, Y., Yu, X. (Bill), 2019. A holistic computational model for prediction of clay suspension structure. Int. J. Sediment Res. 34, 345–354. https://doi.org/10.1016/j.ijsrc.2018.12.002
Gupta, V., Hampton, M.A., Stokes, J.R., Nguyen, A. V., Miller, J.D., 2011. Particle interactions in kaolinite suspensions and corresponding aggregate structures. J.

Colloid Interface Sci. 359, 95–103. https://doi.org/10.1016/j.jcis.2011.03.043
Gupta, V., Miller, J.D., 2010. Surface force measurements at the basal planes of ordered kaolinite particles. J. Colloid Interface Sci. 344, 362–371. https://doi.org/10.1016/j.jcis.2010.01.012
Hattab, M., 2011. Critical state notion and microstructural considerations in clays. Comptes Rendus Mécanique 339, 719–726. https://doi.org/10.1016/j.crme.2011.07.007
Hattab, M., Hicher, P.-Y., 2004. Dilating Behaviour of Overconsolidated Clay. Soils Found. 44, 27–40. https://doi.org/10.3208/sandf.44.4_27
Homola, A.M., Israelachvili, J.N., Gee, M.L., McGuiggan, P.M., 1989. Measurements of and Relation Between the Adhesion and Friction of Two Surfaces Separated by Molecularly Thin Liquid Films. J. Tribol. 111, 675–682. https://doi.org/10.1115/1.3261994
Homola, A.M., Israelachvili, J.N., McGuiggan, P.M., Gee, M.L., 1990. Fundamental experimental studies in tribology: The transition from "interfacial" friction of undamaged molecularly smooth surfaces to "normal" friction with wear. Wear 136, 65–83. https://doi.org/10.1016/0043-1648(90)90072-I
Israelachvili, J.N., 2011. Intermolecular and Surface Forces, Third. ed. Academic Press. https://doi.org/10.1016/C2011-0-05119-0
Itasca, 2015. PFC3D.
Khabazian, M., Mirghasemi, A.A., Bayesteh, H., 2018. Compressibility of montmorillonite/kaolinite mixtures in consolidation testing using discrete element method. Comput. Geotech. 104, 271–280. https://doi.org/10.1016/j.compgeo.2018.09.005
Kumar, N., Zhao, C., Klaassen, A., van den Ende, D., Mugele, F., Siretanu, I., 2016. Characterization of the surface charge distribution on kaolinite particles using high resolution atomic force microscopy. Geochim. Cosmochim. Acta 175, 100–112. https://doi.org/10.1016/j.gca.2015.12.003
Liu, J., Miller, J.D., Yin, X., Gupta, V., Wang, X., 2014a. Influence of ionic strength on the surface charge and interaction of layered silicate particles. J. Colloid Interface Sci. 432, 270–277. https://doi.org/10.1016/j.jcis.2014.06.028
Liu, J., Sandaklie-Nikolova, L., Wang, X., Miller, J.D., 2014b. Surface force measurements at kaolinite edge surfaces using atomic force microscopy. J. Colloid Interface Sci. 420, 35–40. https://doi.org/10.1016/j.jcis.2013.12.053
Ma, K., Pierre, A.C., 1999. Clay Sediment-Structure Formation in Aqueous Kaolinite Suspensions. Clays Clay Miner. 47, 522–526. https://doi.org/10.1346/CCMN.1999.0470415
McBride, M.B., Baveye, P., 2002. Diffuse Double-Layer Models, Long-Range Forces, and Ordering in Clay Colloids. Soil Sci. Soc. Am. J. 66, 1207. https://doi.org/10.2136/sssaj2002.1207
McDowell, G.R., 2002. A simple non-associated flow model for sand. Granul. Matter 4, 65–69. https://doi.org/10.1007/s10035-002-0106-6
McDowell, G.R., 2000. A family of yield loci based on micro mechanics. Soils Found. 40, 133–137.
Mitchell, J.K., Soga, K., 2005. Fundamentals of Soil Behavior, 3rd ed. John Wiley and Sons, Hoboken, New Jersey.
O'Brien, N.R., 1971. Fabric of Kaolinite and Illite Floccules. Clays Clay Miner. 19, 353–359. https://doi.org/10.1346/CCMN.1971.0190603
Pagano, A.G., Magnanimo, V., Weinhart, T., Tarantino, A., 2020. Exploring the micromechanics of non-active clays by way of virtual DEM experiments. Géotechnique 70, 303–316. https://doi.org/10.1680/jgeot.18.P.060
Sjoblom, K.J., 2015. Coarse-Grained Molecular Dynamics Approach to Simulating Clay Behavior. J. Geotech. Geoenviron. ASCE 142, 1–6. https://doi.org/10.1061/(ASCE)GT.1943-5606.0001394.
van Olphen, H., 1963. An Introduction to Clay Colloid Chemistry. John Wiley and Sons, New York.
Volkova, E., Narayanan Nair, A.K., Engelbrecht, J., Schwingenschlögl, U., Sun, S.,

Stenchikov, G., 2021. Molecular Dynamics Modeling of Kaolinite Particle Associations. J. Phys. Chem. C 125, 24126–24136. https://doi.org/10.1021/acs.jpcc.1c06598

Wang, Y.-H., Siu, W.-K., 2006. Structure characteristics and mechanical properties of kaolinite soils. I. Surface charges and structural characterizations. Can. Geotech. J. 43, 587–600. https://doi.org/10.1139/t06-026

Westerberg, B., 1995. Lerors mekaniska egenskaper. Lulea University of Technology.

Wood, D.M., 1990. Soil Behaviour and Critical State Soil Mechanics. Cambridge University Press.

Wroth, C.P., 1987. The behaviour of normally consolidated clay as observed in undrained direct shear tests. Géotechnique 37, 37–43. https://doi.org/10.1680/geot.1987.37.1.37

Yao, M., Anandarajah, A., 2003. Three--Dimensional Discrete Element Method of Analysis of Clays. {ASCE} J. Eng. Mech. 129, 585–596.

Zen, A., Bui, T., Bao Le, T.T., Tay, W.J., Chellappah, K., Collins, I.R., Rickman, R.D., Striolo, A., Michaelides, A., 2022. Long-Range Ionic and Short-Range Hydration Effects Govern Strongly Anisotropic Clay Nanoparticle Interactions. J. Phys. Chem. C 126, 8143–8151. https://doi.org/10.1021/acs.jpcc.2c01306